Soft Matter

ARTICLE TYPE

Cite this: DOI: 00.0000/xxxxxxxxxx

Nanoparticle dynamics in hydrogel networks with controlled defects

Katie A. Rose,[a] Emanuele Marino,[b,c] Christopher S. O'Bryan,[d] Christopher B. Murray,[b,e] Daeyeon Lee,[a*] and Russell J. Composto[a,e,f*]

Received Date
Accepted Date

DOI: 00.0000/xxxxxxxxxx

The effect of nanoscale defects on nanoparticle dynamics in defective tetra-poly(ethylene glycol) (tetra-PEG) hydrogels is investigated using single particle tracking. In a swollen nearly homogeneous hydrogel, PEG-functionalized quantum dot (QD) probes with a similar hydrodynamic diameter ($d_h =$ 15.1 nm) to the mesh size ($\langle \xi_s \rangle = 16.3$ nm), are primarily immobile. As defects are introduced to the network by reaction-tuning, both the percentage of mobile QDs and the size of displacements increases, although a large portion of the QDs remain immobile. To probe the effect of nanoparticle size on dynamics in defective networks, the transport of $d_h = 47.1$ nm fluorescent polystyrene (PS) and $d_h = 9.6$ nm PEG-functionalized QDs is investigated. The PS nanoparticles are immobile in all hydrogels, even in highly defective networks with an open structure. Conversely, the smaller QDs are more sensitive to perturbations in the network structure with an increased percentage of mobile particles and larger diffusion coefficients compared to the larger QDs and PS nanoparticles. The differences in nanoparticle mobility as a function of size suggests that different sized particles probe different length scales of the defects, indicating that metrics such as the confinement ratio alone cannot predict bulk dynamics in these systems. This study provides insight into designing hydrogels with controlled transport properties, with particular importance for degradable hydrogels for drug delivery applications.

1 Introduction

Hydrogels are 3D polymeric networks composed of polymer strands connected by physical or chemical crosslinks. Their unique porosity, swelling capabilities, tunable mechanical properties, and biocompatibility has led to their widespread use in biomedical applications ranging from tissue engineering scaffolds,[1–3] wound dressings,[4,5] and drug delivery platforms.[2,6] In many of these applications, understanding and controlling the transport properties of nanoparticles, pharmaceuticals, and other cargo within these hydrogels is imperative. Understanding the dynamics of various molecules such as small molecule drugs, peptides, and proteins as well as molecule-conjugated nanoparticles is particularly important to the efficacy of degradable hydrogels in drug delivery applications. Initially, either high crosslinking density or covalent attachment to the network traps the molecule of interest or molecule-carrying nanoparticle. The network can then be degraded through interactions with its environment including enzymatic degradation or hydrolysis, or degradation via external stimuli such as UV or light.[7–9] As the hydrogel structure devolves into a less densely crosslinked network, the mobility of the initially trapped component, molecule or nanoparticle, within the network increases, resulting in eventual diffusion through and then out of the hydrogel network. The dynamics of the probe of interest within the hydrogel depends on the network pore size, network heterogeneity, the size of the probe, and interaction between the probe and the polymer network. Predicting the mobility of probes during hydrogel degradation, including how network defects impact particle mobility, is necessary to accurately control the drug elution profile in biomedical applications.

While a homogeneous network is attractive for modeling, synthetic and biological hydrogels are far from ideal at the nanoscale. Two main sources of heterogeneity come from 1) spatial nanoscale heterogeneity and 2) topological defects. Spatial heterogeneity reflects local variations in the crosslinking density

[a] Department of Chemical and Biomolecular Engineering, University of Pennsylvania, Philadelphia, PA, 19104
[b] Department of Chemistry, University of Pennsylvania, Philadelphia, PA, 19104
[c] Dipartimento di Fisica e Chimica, Università degli Studi di Palermo, Palermo, Italy, 90123
[d] Department of Mechanical and Aerospace Engineering, University of Missouri, Columbia, MO, 65201
[e] Department of Materials Science and Engineering, University of Pennsylvania, Philadelphia, PA, 19104
[f] Department of Bioengineering, University of Pennsylvania, Philadelphia, PA, 19104
* Corresponding author information. Email: daeyeon@seas.upenn.edu, composto@seas.upenn.edu
† Electronic Supplementary Information (ESI) available.

resulting from the stochastic process of polymerization and network formation, which depends on the monomer concentration, crosslinker concentration, temperature and choice of solvent.[10] As the network forms, crosslinking occurs non-uniformly leading to a distribution of the distance between crosslinks, or mesh size (ξ). Scattering based techniques, including light scattering, small angle x-ray scattering, and neutron scattering are primarily used to identify and measure spatial heterogeneities.[11–13] Additionally, these spatial heterogeneities are further enhanced upon swelling because highly crosslinked regions restrict swelling while loosely crosslinked regions take up more solvent, further pronouncing the differences in crosslinking density.[14] Topological defects include dangling ends, where one end of the growing chain does not integrate into the continuous network, and closed loops, where a chain connects to the same crosslinking junction. Spectroscopic techniques including nuclear magnetic resonance (NMR) have been used to characterize dangling ends and loops.[15,16] Topological defects have a pronounced effect on the mechanical properties of hydrogels, as their presence effectively decreases the number of elastically effective crosslinks in the network.

Nanoscale spatial heterogeneity greatly affects particle dynamics in hydrogels. In polyacrylamide gels, the heterogeneous network formed by free-radical polymerization results in a wide distribution of mesh sizes with regions of low and high crosslinking density. In turn, this distribution creates local environments that impacts nanoparticle dynamics and results in non-Gaussian displacements as measured through single particle tracking methods.[17,18] Similarly, in κ-Carrageenan gels, polystyrene nanoparticles exhibit an order of magnitude lower diffusion coefficient in dense network regions compared to the more open network.[19] Single particle tracking methods are particularly useful in investigating dynamics in heterogeneous media because they can distinguish between these slow and fast modes of particle dynamics resulting from the spatial distribution of crosslinks. In this way, single particle tracking can reveal the nanoscale structure of hydrogels.

Whereas the networks of many synthetic and biological hydrogels are naturally heterogeneous, synthesizing a polymer network with controlled heterogeneity is more challenging. Recently, nearly ideal networks have been formed through the crosslinking of two tetra-poly(ethylene glycol) (PEG) macromers with succinimidyl glutarate (TPEG-SG) and amine (TPEG-A) end-group functionalities.[20] The network structures have a narrow distribution of mesh sizes because of the underlying structure of the 4-arm macromers and the reaction conditions.[21] In the fully gelled structure, the mesh size (ξ) of the hydrogel is dictated by the molecular weight of the 4-arm tetra-PEG macromonomer. The presence of topological defects such as loops are limited as the end groups of each tetra-PEG macromonomer are mutually reactive.[22] For optimized reaction conditions (ionic strength and pH), the gelation kinetics are reaction-limited such that tetra-PEG macromers are able to diffuse and create a homogeneous solution prior to reacting.[23,24] Additionally, to achieve high reaction efficiency, the crosslinking of the TPEG-SG and TPEG-A must occur at a much faster rate than the hydrolysis of the moisture sensitive NHS-ester end group of the TPEG-SG macromonomer. By controlling the hydrolysis of the NHS-ester end group, the reaction efficiency can be controlled as the TPEG-SG is unable to incorporate into the network resulting in a dangling end.[23] In most applications, the hydrolysis of the TPEG-SG is undesirable because the goal is to form nearly ideal networks with uniform crosslinking density. However, controlling the hydrolysis of the TPEG-SG macromonomer offers a unique approach to control the defects in the network. The mechanical and structural properties of these incomplete networks have been previously studied, including the elastic modulus,[25] elongation ratio,[26], the fracture energy,[27,28] and the correlation length.[24] Recent studies by Khairulina et al have examined the electrophoretic mobility of DNA in these defective gels, further highlighting their use as model defective polymer networks to measure probe dynamics.[29,30] Sheth et al have also examined the bulk release of proteins from a degradable tetra-PEG with a degradable bi-functional PEG crosslinker.[8] While these studies are useful in understanding the bulk release kinetics, single particle tracking allows for the measurement of individual trajectories, allowing for a better understanding of the relationship between nanoparticle mobility and the different local environments resulting from different extents of degradation.

This study seeks to understand the relationship between the tetra-PEG hydrogel network structure, namely the average mesh size measured from macroscopic properties, and nanoscale transport through networks with increasing mesh size as defects are added. To control defects, TPEG-SG (20 kg/mol) is hydrolyzed in buffer solution for 15 to 75 minutes. Upon mixing TPEG-SG with TPEG-A (20 kg/mol), the number of defects and the average mesh size increases as hydrolysis time increases. These increases in network defects are captured by changes in the macroscopic properties of the network, as the plateau storage modulus, G'_p, decrease from $\sim$ 2400 Pa to $\sim$ 90 Pa, and the average swollen mesh size, $\langle \xi_s \rangle$, increase from 16.3 nm to 50.3 nm, consistent with an increase in network defects. The effects of nanoscale defects on particle dynamics were investigated using PEG-functionalized CdSe/CdS quantum dots (15.1 nm) dynamics in networks corresponding to swollen $\langle \xi_s \rangle$ of 16.3 nm, 21.3 nm, 27.9 nm and 50.3 nm. In all networks, the majority of the QDs are immobile, with small increases in the percentage of mobile particles and the particle displacements with increasing defects. In addition, the effect of nanoparticle probe size on transport is investigated for larger 47.1 nm fluorescent polystyrene (PS) nanoparticles, and smaller 9.6 nm PEG-functionalized CdSe/CdS quantum dots. While large PS particles exhibit no mobility in all networks, smaller QDs are more sensitive to the addition of defects with increased mobility and displacements compared to their larger 15.1 nm QD counterparts in identical networks. Furthermore, the confinement of the particle due to the average mesh size alone cannot be used to predict bulk dynamics as shown by comparing the dynamics of the two sizes of QDs in networks of comparable confinement ratios. Overall, this work demonstrates the effect of nanoparticle size on probe mobility in controlled defective networks, key for understanding particle dynamics in degradable hydrogel networks.

2 Materials and methods

2.1 Materials

4-arm tetra-polyethylene glycol (PEG) succinimidyl glutarate (TPEG-SG) and 4-arm tetra-PEG amine (TPEG-A), both 20 kg/mol, are purchased from Jenkem Technology USA. Thiol-PEG, 5 kg/mol, is purchased from Creative PEGWorks. Citric acid, sodium phosphate dibasic, sodium phosphate monobasic monohydrate, and disodium hydrogen phosphate heptahydrate are purchased from Sigma Aldrich. 35 mm glass bottom culture dishes are purchased from Avantor, made by Matsunami Glass. Fluorescent polystyrene spheres are purchased from Bangs Labs.

2.2 Probe synthesis and modification

Two sizes of highly photoluminescent QDs are synthesized using the procedure outlined by Hanifi et al.[31,32] We measure the average diameters of the two sets of core/shell CdSe/CdS particles using transmission electron microscopy (TEM) to be $d = 9.6$ nm and 5 nm (see ESI †). To disperse the QDs in water, a ligand exchange using a 5 kg/mol thiol-PEG is completed as previously reported.[33] Briefly, oleic acid capped QDs are added to thiol-PEG toluene solution, with thiol-PEG in excess and vigorously stirred overnight. PEG-functionalized QDs are precipitated out of solution and centrifuged into a pellet. The QD pellet is then dried overnight before dispersing in deionized water (10 mL) prior to running through a 30 kDa centrifugal filter. The PEG-functionalized QD hydrodynamic diameters are determined to be $d_h = 15.1$ and 9.6 nm by measuring the diffusion coefficient in solutions of glycerol-water (70, 80, 90 v%) at 20°C and fitting the data to the Stokes-Einstein relationship (see ESI †). Fluorescent polystyrene spheres (manufacturer reported diameter = 42 nm) are purchased from Bangs Laboratory and used as received. The hydrodynamic diameter of the polystyrene particles in water is determined through dynamic light scattering (DLS) to be 47.1 nm (see ESI †).

2.3 Tetra-PEG hydrogel synthesis

Tetra-PEG hydrogels are prepared by dissolving TPEG-SG and TPEG-A in stoichiometric amounts (40 mg/mL or 45 mg/mL) in phosphate (pH 7.4, 50 mM) and phosphate-citrate buffers (pH 5.8, 50 mM), respectively. To create defects in the hydrogel, TPEG-SG is added to the phosphate buffer solution and incubated for a predetermined amount of time, t_{hyd}, ranging from 15 to 75 minutes, prior to mixing with the TPEG-A solution. For $t_{hyd} = 0$ minutes, TPEG-SG and TPEG-A solutions are mixed immediately after preparation. For particle tracking studies, tetra-PEG solutions are added in equal amounts into a microcentrifuge tube with the nanoparticle probe solution, mixed for 30 seconds, and deposited onto a glass bottom petri-dish. Samples are sealed and allowed to fully gel overnight in a second petri-dish with ample water to create a humid environment to prevent evaporation. Hydrogels are then swollen for 24 hours in nanoparticle rich solution. Once hydrated, hydrogels are detached from the surface to release any residual stress from swelling. All solution is then removed from the glass bottom petri-dish, and the gel is allowed to re-adhere to the surface before subsequent swelling in probe solution for 24 hours prior to particle tracking.

All studies are conducted at the critical overlap concentration, $c*$, which for similar 20 kg/mol 4-armed tetra-PEG macromers as has been previously determined to be 40 mg/mL via viscometry.[11] For the rheology and swelling studies, tetra-PEG solutions are prepared at $c*$. For particle tracking studies, the initial concentration of the TPEG solutions is prepared at 45 mg/mL to account for the addition of the nanoparticle probe solution, resulting in a final polymer concentration in the gel of 40 mg/mL, or $c*$.

2.4 Tetra-PEG hydrogel characterization

Oscillatory rheometry is performed on an AR2000ex (TA Instruments) fitted with stainless steel (20 mm diameter cone, 59 min 42 s) cone and plate geometry. A time sweep (1% strain, 1 Hz) to probe changes in the storage, G', and loss, G'', moduli during gelation is conducted for eight hours at 20 °C. To minimize evaporation, all gels are polymerized in a solvent trap. All samples ($t_{hyd} = 0, 15, 30, 45, 60$ and 75 minutes) are run in duplicate on separate days. Data is offset due to the time to prepare the sample on the rheometer after mixing.

To measure changes in swelling behavior based on network defects, a series gels are synthesized for $t_{hyd} = 0, 15, 30, 45, 60,$ and 75 minutes. Samples are allowed to gel overnight in a sealed chamber to ensure complete gelation. Following gelation, as prepared samples are immersed in a deionized water bath for 48 hours to remove unreacted monomer and reach swelling equilibrium. Equilibrium swollen hydrogel samples are subsequently removed from the water bath, lightly dabbed with a Kimwipe to remove surface water, and weighed to obtain the weight of the swollen hydrogel, W_s. Gels are then dried for a week to removal all water from the sample prior to re-weighting to obtain a dried sample weight, W_d. The mass swelling ratio, Q_m is calculated as follows,

$$Q_m = \frac{W_s - W_d}{W_d} \tag{1}$$

The mass swelling ratio can be converted to the volumetric swelling ratio, Q_v, using the polymer and solvent densities,

$$Q_v = Q_m * \frac{\rho_p}{\rho_s} + 1 \tag{2}$$

where ρ_p and ρ_s are the polymer and solvent densities, respectively. The polymer density for PEG is 1.129 g/cm^3 and the density of water is 0.9982 g/cm^3.

The mesh size for tetra-PEG hydrogels can be estimated using the elastic blob model,

$$G' = \frac{k_b T}{\xi^3} \tag{3}$$

where k_b is the Boltzman constant, T is temperature measured in Kelvin, and G' is the storage modulus taken from rheology. The mesh size for a swollen hydrogel uses the same scaling, but uses the swollen storage modulus, G'_s, which can be calculated as follows,[34]

$$G'_s = G' \frac{Q_{v,s}^{-1/3}}{Q_v^{-1/3}} \tag{4}$$

where Q_v is the as prepared volumetric swelling ratio and $Q_{v,s}$ is the volumetric equilibrium swelling ratio.

In a swollen hydrogel network, the confinement ratio, or the ratio of the particle hydrodynamic diameter to mesh size, $\langle \xi_s \rangle$, is defined as follows,

$$CR = d_h / \langle \xi_s \rangle \tag{5}$$

where d_h is the hydrodynamic diameter of the nanoparticle probe measured from single particle tracking or dynamic light scattering, and $\langle \xi_s \rangle$ is the swollen mesh size calculated from Eqs. 4 and 3.

2.5 Single particle tracking (SPT) analysis

Quantum dot (QD) and polystyrene (PS) nanoparticle dynamics in tetra-PEG hydrogels are imaged using an inverted Nikon Eclipse Ti optical microscope equipped with a 100x, 1.49 NA oil immersion objective (Nikon). Videos of a 1200x1200 pixel region of interest are collected for 30 seconds (33.3 fps), using a cooled sCMOS camera (Prime 95b, Photometrics). Particle locations are fit by a 2-D Gaussian and trajectories linked in Fluorescence Image Evaluation Software for Tracking and Analysis (FIESTA).[35] Trajectories were manually checked for accuracy and correct linking prior to subsequent analysis.

The average distance traveled by a particle over a given lag time can be described by the mean squared displacement (MSD) as given by,

$$MSD(\tau) = \langle \Delta r(\tau)^2 \rangle_t = \langle [r(t+\tau) - r(t)]^2 \rangle_t \tag{6}$$

where τ is the lag time, $r(t)$ is the position of the particle at absolute time t, and $\langle \rangle_t$ denotes the averaging over time. The MSDs are calculated using msdanalyzer in MATLAB with additional analysis conducted using house code.[36]

The self portion of the van Hove distribution function describes the probability distribution of probe displacements at a given τ. Namely, the probability of finding a particle i at a distance $r + \Delta r$ at a given time $t + \tau$ as follows,

$$G(\Delta r, \tau) = \frac{1}{N} \langle \sum_{i=1}^{N} \delta(r_i(t) - r_i(t+\tau) - \Delta r) \rangle_t \tag{7}$$

where δ is the Dirac delta function. The absolute values of Δr are used to account for positive and negative portions of the van Hove to easily visualize deviations from a Gaussian functional form.

Furthermore, the non-Gaussian parameter, α_{NG}, provides a quantifiable measure of the deviation of the van Hove distribution from Gaussian behavior,[37]

$$\alpha_{NG} = \frac{\langle \Delta r^4(\tau) \rangle}{3 \langle \Delta r^2(\tau) \rangle^2} - 1 \tag{8}$$

where $\langle \Delta r^2(\tau) \rangle$ and $\langle \Delta r^4(\tau) \rangle$ second and fourth moments of the displacements.

3 Results and discussion

Nanoparticle dynamics is studied as a function of increasing average mesh size due to the addition of network defects using single particle tracking. Network defects are modulated via reaction-tuning, achieved by incubating tetra-PEG succinmidyl glutarate (TPEG-SG) macromers for various times (t_{hyd}) to hydrolyze the NHS end-groups prior to mixing with the tetra-PEG amine (TPEG-A). This creates a range of network structures, from a highly crosslinked, small mesh size, nearly homogeneous network at $t_{hyd} = 0$ minutes to a highly defective network with a large mesh size that forms a more heterogeneous network at $t_{hyd} = 75$ minutes. Macroscopic properties as a function of t_{hyd} are characterized via rheology and swelling measurements. First, we investigate PEG-functionalized quantum dot (15.1 nm) dynamics as a function of increasing mesh size due to the incorporation of defects. Second, we compare nanoparticle dynamics in the same hydrogel networks as a function of probe size for polystyrene (47.1 nm) and PEG-functionalized quantum dot (9.6 nm) probes.

3.1 Characterization of reaction-tuned Tetra-PEG hydrogels

In this study, tetra-PEG hydrogels are formed by reacting tetra-PEG succinimidyl glutarate (TPEG-SG) with an *N*-Hydroxysuccinimide (NHS) ester functionality, and tetra-PEG amine (TPEG-A) at the overlap concentration, $c*$. The gelation of tetra-PEG hydrogels is schematically represented in Figure 1. To introduce defects and increase the mesh size, TPEG-SG is incubated in buffer for different lengths of time, $t_{hyd} = 0$ to 75 minutes. For $t_{hyd} = 0$ minutes, the gelation has a high reaction efficiency, with the majority of the TPEG-SG and TPEG-A reacting to create an amide bond with a reaction efficiency of $\sim$ 90% as reported by others.[38] Conversely, defective networks can be formed by partially degrading the TPEG-SG, $t_{hyd} > 0$ minutes. The NHS-ester functionality of the TPEG-SG is moisture sensitive and incubation of the TPEG-SG in buffer leads to hydrolysis of the NHS-ester. The hydrolysis of similar tetra-PEG NHS functionalized macromers is pH sensitive, with an estimated half-life of the activated ester of 210 minutes at pH 5.8 and 130 minutes at pH 7.[23] Reported experimental rates of TPEG-SG hydrolysis deviate from theoretical predictions due to the increased acidity of the solution upon the hydrolysis of the NHS group, which slows down the reaction.[23] The resulting carboxylic acid group is unable to covalently crosslink with the amine group on the other tetra-PEG macromonomer, resulting in defects at those spatial locations in the hydrogel. While the dangling ends of each tetra-PEG macromonomer (carboxylic acid and amine) are charged at near physiological pH, electrostatic interactions between the two dangling ends do not appear to create a network as measured by studying particle dynamics solutions of 1) fully hydrolyzed TPEG-SG and 2) fully hydrolyzed TPEG-SG and TPEG-A (see ESI †). By increasing the incubation time of the TPEG-SG, t_{hyd}, prior to mixing with the TPEG-A, we expect the number of spatial defects to increase, resulting in increased mesh sizes and increased network heterogeneity.

Rheology is used to quantify macroscopic changes in the network as a function of t_{hyd} with a focus on changes in 1) the storage modulus, G', and 2) the gel point, t_{gel}. G' is an indication of a polymer network's ability to store deformation energy in an elastic manner, which is directly related to the number of crosslinks

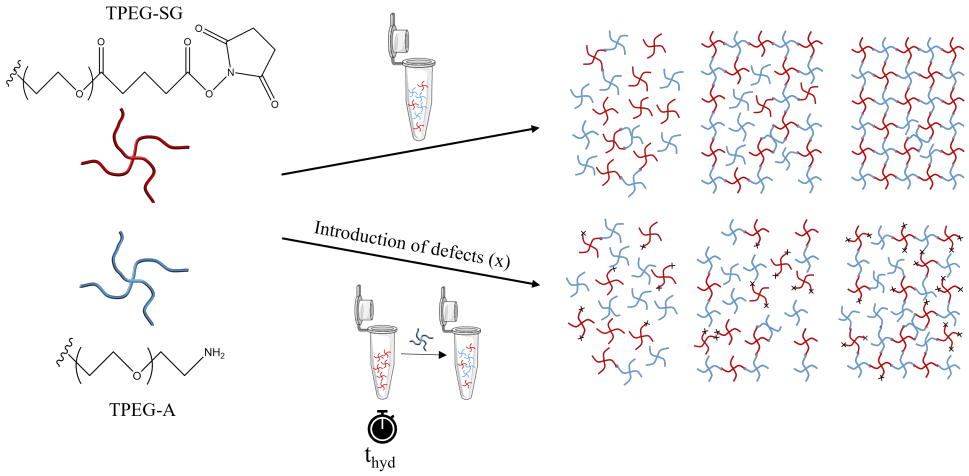

Fig. 1 Schematic of tetra-PEG gelation via a condensation reaction of tetra-PEG succinimidyl glutarate (TPEG-SG) and amine (TPEG-A) macromers. At $t_{hyd} = 0$ minutes, a nearly ideal network forms. At $t_{hyd} > 0$ minutes, the hydrolysis of the NHS end group results in defective arms on the TPEG-SG (denoted by x), resulting in defective networks.

in the network. Therefore, changes in G' can be used as to determine how the network structure is changing as defects are introduced into the network. Additionally, the crossover of the storage, G', and loss, G'', modulus indicates the onset of network formation, or the gel point, t_{gel}. While not a direct measure of the evolution of the network structure, an increase in t_{gel} indicates a decrease in gelation kinetics as the time to create a percolated network is longer.

Figure 2(left) shows representative G' curves during tetra-PEG gelation for reaction-tuning times $t_{hyd} = 0, 15, 30, 45, 60$ and 75 minutes. From the storage modulus measurements, the plateau storage modulus, G'_p, is determined for each sample by denoting its value when the G' changes less that 1% over a ten minute period. Figure 2 (right) shows that G'_p decreases from $\sim$ 2400 Pa to $\sim$ 90 Pa as t_{hyd} increases from 0 to 75 minutes, indicating that the hydrolysis of the TPEG-SG prior to crosslinking reduces the modulus by $\sim$ 24 times because of the reduction in crosslinking density.

Additionally, changes in the gelation kinetics is determined from the crossover of the storage and loss (G'') moduli ($G' > G''$), t_{gel}. While the exact gel point, t_{gel}, is generally frequency independent and therefore needs to be measured at multiple frequencies, the crossover of G' and G'' can be used as a close approximation.[39–41] A longer t_{hyd} results in an increased t_{gel}, with $t_{gel} = 24$ minutes at $t_{hyd} = 0$ minutes and $t_{gel} = 93.5$ minutes in the most defective network, $t_{hyd} = 75$ minutes. The monotonic increase in t_{gel} as a function of t_{hyd} indicates decreased gelation kinetics with the partial hydrolysis of the TPEG-SG macromonomer. This trend is expected, as the partially hydrolyzing the NHS of TPEG-SG macromers are unable to contribute to the growing network, increasing the time for a percolated network to form. In Figure 2, only G' is shown for readability, though examples of the crossover of G' and G'' for $t_{hyd} = 0$ and 15 minutes can be found in Supporting Information, along with the average t_{gel} for each t_{hyd}. In addition to the samples in Figure 2, $t_{hyd} = 90$ minutes is also measured. While the sample is a gel ($G' > G''$) at long times ($t_{gel} \sim 225$ minutes), the low G' ($\sim$ 7 Pa) made for a weak gel that is unable to be handled without breakage, and is therefore excluded from the rest of the study. At even longer t_{hyd}, 105 minutes, there is no crossover indicating that a substantial fraction of the TPEG-SG arms have hydrolyzed such that a percolated network cannot form.

Hydrogel swelling can also be used to further characterize the extent of crosslinking. As t_{hyd} increases, the mass swelling ratio, Q_m, monotonically increases from 45 at $t_{hyd} = 0$ minutes to 103 at $t_{hyd} = 75$ minutes (Supporting Information). The swelling behavior of a hydrogel is in part related to the crosslinking density; generally, the higher the crosslinking density, the lower the swelling ratio.[42] The trends seen in the swelling behavior of the hydrogels complement that seen in rheology, where the most highly crosslinked networks (high G') have the lowest Q_m and vice versa.

The average mesh size, or the distance between crosslinks, $\langle\xi\rangle$, is often used as a parameter to understand probe dynamics within a hydrogel. In this work, we calculate the average mesh size of the hydrogel samples using elastic blob theory given by $G' \simeq k_b T/\xi^3$. Figure 3 shows how the average mesh size increases as t_{hyd} increases for the as prepared, $\langle\xi\rangle$, and equilibrium swollen, $\langle\xi_s\rangle$, gels. First, as t_{hyd} increases, $\langle\xi\rangle$ and $\langle\xi_s\rangle$ increases for both the as prepared and swollen gels. For the as prepared, this results in an increase in $\langle\xi\rangle$ from 11.8 nm to 35.5 nm as t_{hyd} increases from 0 to 75 minutes. Second, for a given t_{hyd}, the swollen hydrogel has a larger $\langle\xi_s\rangle$ than that of the as prepared gel, $\langle\xi\rangle$. For example, at $t_{hyd} = 0$ minutes, or the most ideal network structure, the average mesh size increases from 11.8 nm ($\langle\xi\rangle$) to 16.3 nm ($\langle\xi_s\rangle$), which is expected due to the presence of a small number of defects leading to an increased $\langle\xi_s\rangle$. Similar to the as prepared samples, the $\langle\xi_s\rangle$ increases with increasing t_{hyd} from 16.3 nm in the most homogeneous hydrogel ($t_{hyd} = 0$ minutes) to 50.3 nm in the most defective hydrogel ($t_{hyd} = 75$ minutes). It is worth noting that these calculations give an average mesh size, which does

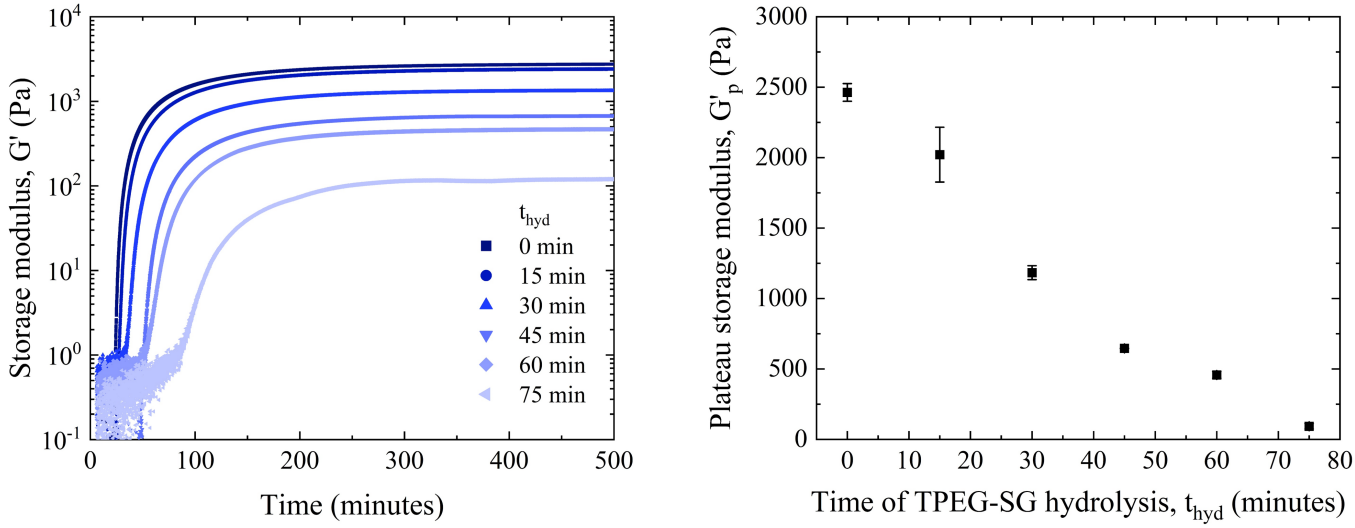

Fig. 2 Storage modulus, G', during the gelation of a tetra-PEG hydrogels with increasing t_{hyd} (left). Plateau storage modulus, G'_p, as a function of t_{hyd} (right). Error bars come from duplicate runs ($n = 2$).

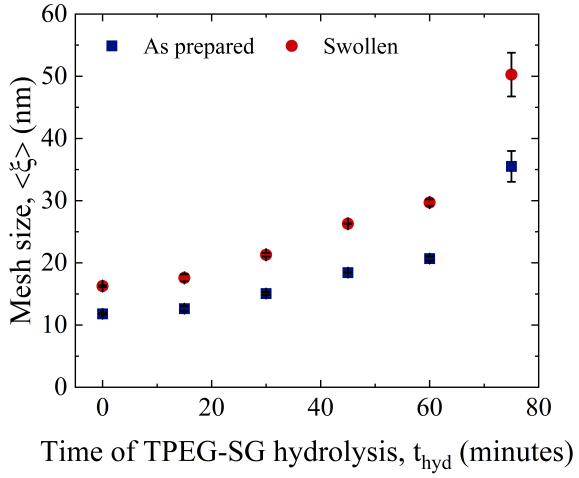

Fig. 3 Average mesh size calculated from elastic blob theory, before (as cast, $\langle\xi\rangle$) and after swelling ($\langle\xi_s\rangle$) as a function of t_{hyd}. Error bars are from the measurement of G' and represent duplicates taken on separate days.

not represent the range or distribution of ξ in a heterogeneous network. Rather than a uniform ξ across the network, some regions will contain larger ξ where defect density is high, creating spatial heterogeneity. This heterogeneity will impact nanoparticle dynamics, in particular the distribution of mean squared displacements and the non-Gaussian parameter as described below.

3.2 Single particle tracking of PEG-functionalized quantum dots (15.1 nm) in hydrogels of increasing mesh size

Single particle tracking is used to examine the dynamics of hydrodynamic diameter (d_h) = 15.1 nm PEG-functionalized QDs in tetra-PEG hydrogels. The dynamics of nanoparticles are explored in four t_{hyd} networks, corresponding to $t_{hyd} = 0, 30, 60$ and 75 minutes, or $\langle\xi_s\rangle = 16.3, 21.3, 29.7$ and 50.3 nm, respectively. These values are chosen to investigate a wide range of $\langle\xi_s\rangle$ and therefore confinements of the nanoparticles probes, as well as a range of different local environments dependent on the spatial locations of the defects. Furthermore, the impact of defects on the microstructure is most pronounced in the swollen networks; given that the majority of hydrogels are used in their fully swollen state, probing the nanoparticle transport in swollen hydrogel structures is highly relevant for practical applications. The confinement ratio, $CR = d_h/\langle\xi_s\rangle$, a comparison of the size of the nanoparticle compared to the average mesh size, can be used as an initial parameter to gauge a particle's mobility in the hydrogel. In a nearly homogeneous network, particles much larger than the mesh size ($CR >> 1$) are permanently trapped in the network.[43] While particles slightly larger than the mesh size ($CR > 1$) can escape a primary cage due to fluctuations in the polymer network as predicted by nanoparticle hopping, it is unlikely to observe nanoparticle mobility as a function of hopping due to the resolution of the instrument (10's nm). Conversely, for nanoparticles smaller than the mesh size ($CR < 1$), particles can move between neighboring

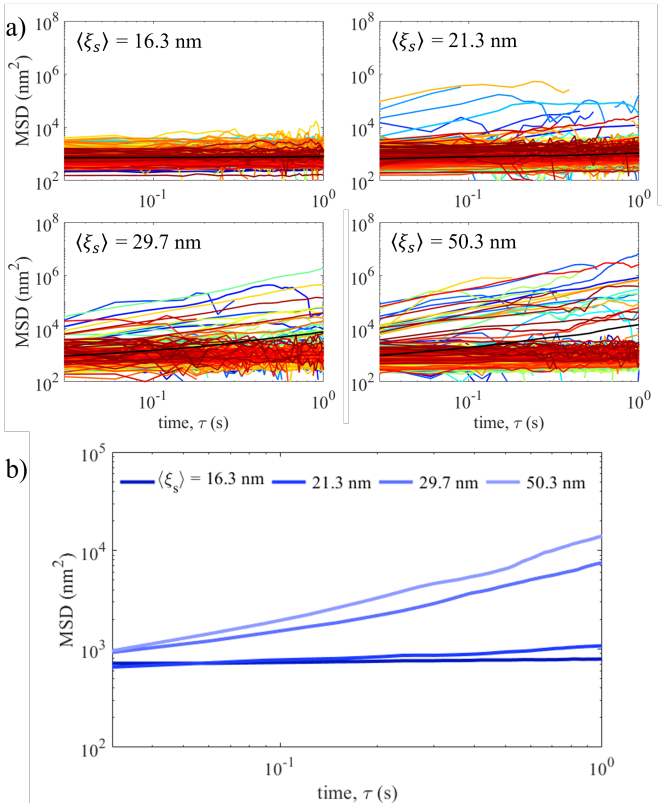

Fig. 4 a) Mean squared displacements (MSD) of individual 15.1 nm PEG-functionalized quantum dot (QD) nanoparticle trajectories in increasingly defective tetra-PEG hydrogels. Black lines are the ensemble average of all particle MSDs. b) Ensemble average MSDs for $\langle\xi_s\rangle = 16.3$ nm, 21.3 nm, 29.7 nm and 50.3 nm.

meshes, resulting in mobile nanoparticles. While this is true in a homogeneous network, heterogeneous networks are much more complicated due to the range of mesh sizes around an average $\langle\xi_s\rangle$. In defective hydrogel networks, the mesh size is heterogeneous throughout the gel. For the 15.1 nm QD, the confinement ratio ranges from $CR = 0.93$ in the most highly crosslinked network, $\langle\xi_s\rangle = 16.3$ nm, to 0.30 in the most defective network, $\langle\xi_s\rangle = 50.3$ nm, as seen in Table 1.

At $\langle\xi_s\rangle = 16.3$ nm ($CR = 0.93$), the majority of the QDs are immobile as indicated by a near constant value of the mean squared displacement (MSD) shown in Figure 4. As $\langle\xi_s\rangle$ increases from 16.3 nm to 21.3 nm, most of the particles remain localized though there is a small number of particles that escape their cages and explore lower crosslinked regions as indicated by the individual particles with a large MSD. Because the percentage of mobile particles is small, the ensemble average MSD curves for the $\langle\xi_s\rangle = 16.3$ nm and 21.3 nm cases are similar as shown in Figure 4. As more defects are added to the network, $\langle\xi_s\rangle = 29.7$ nm, there is an increase in both the fraction of mobile particles and the size of the region a single particle explores, resulting in an increased ensemble average MSD (see ESI †). Similarly, at $\langle\xi_s\rangle = 50.3$ nm there is a slight increase in the ensemble MSD due to an increased number of mobile particles (6.6% to 7.5%) though the change is small. While there are mobile 15.1 nm QDs present in all gels with the exception of $\langle\xi_s\rangle = 16.3$ nm, the overwhelming majority

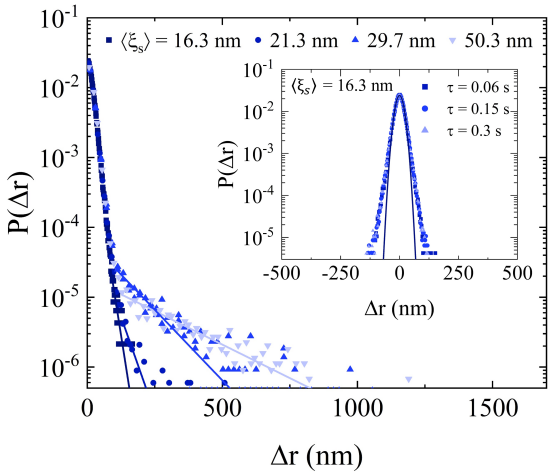

Fig. 5 van Hove distribution function of 15.1 nm quantum dots in $t_{hyd} = 0, 30, 60$ and 75 minutes at $\tau = 0.15$ seconds. Lines indicate fits to the exponential tails. Inset is the van Hove distribution function for $t_{hyd} = 0$ minutes at $\tau = 0.06, 0.15$ and 0.3 seconds. The line represents a Gaussian fit to $\tau = 0.06$ seconds.

of the population are immobile even in the most defective gels. For example, at $\langle\xi_s\rangle = 50.3$ nm, only $\sim 7.5\%$ of the particles are mobile indicating that the majority are localized. This indicates that while defects are modifying the network structure, the length scales of the mesh even with the incorporation of defects are not large enough to allow for most 15.1 nm QDs to undergo large displacements.

In addition to the individual and ensemble average MSDs, the van Hove distribution function can examine probe mobility. For identical particles diffusing through a homogeneous fluid, the distribution can be fit to a Gaussian functional form. However, deviations from a Gaussian such as the emergence of long exponential tails representing larger than predicted displacements indicate that probe particles are not experiencing homogeneous local environments.[44] These exponential tails are seen in a variety of heterogeneous polymer networks and glasses; in heterogeneous hydrogels in particular, these tails are attributed to particles escaping local cages and exploring less dense regions.[17,18,45] For a given τ, these tails can be fit with an exponential decay function which gives the characteristic length scale, λ, corresponding to the displacements of mobile particles within the exponential tail,

$$p(\Delta r, \tau) \sim \exp(-|\Delta r|/\lambda(\tau)) \quad (9)$$

As shown in Figure 5, the van Hove distribution function for the 15.1 nm QDs in the $\langle\xi_s\rangle = 16.3$ nm network deviates slightly from the Gaussian functional form, with an increased probability for large displacements (Fig. 5, inset). Additionally, the displacements of the 15.1 nm QDs within the $\langle\xi_s\rangle = 16.3$ nm network do not increase with increasing τ, indicating that the particles are immobile at the time scales of measurement. The resulting characteristic length scale of the exponential tail at $\tau = 0.15$ seconds, λ, is 17.6 nm indicating that these displacements are small. The few mobile particles at $\langle\xi_s\rangle = 21.3$ nm undergo limited large-scale

Table 1 Confinement ratio ($CR = d_h/\langle\xi_s\rangle$) for the PEG-functionalized 9.6 nm and 15.1 QDs and 47.1 nm polystyrene as a function of reaction-tuning tetra-PEG hydrogels.

t_{hyd} (minutes)	$\langle\xi_s\rangle$, (nm)	CR, 15.1 nm QD	CR, 47.1 nm PS	CR, 9.6 nm QD
0	16.3	0.93	2.89	0.59
30	21.3	0.71	2.21	0.45
60	29.7	0.51	1.58	0.32
75	50.3	0.30	0.94	0.19

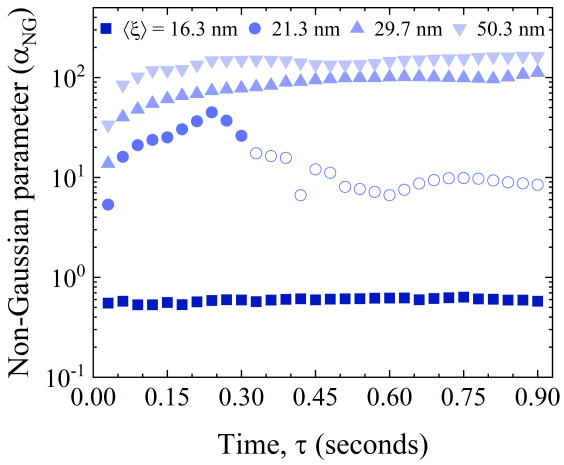

Fig. 6 Evolution of the non-Gaussian parameter (α_{NG}) at different lag times, τ, for increasingly defective tetra-PEG hydrogels. Open circles are used as a guide to the eye to show the decrease in α_{NG} with increasing lag time, τ, for $\langle\xi_s\rangle = 21.3$ nm

.

displacements as indicated by the low probabilities with $\lambda = 39.5$ nm (Fig. 5). This trend of increased displacements and λ continues for $\langle\xi_s\rangle = 29.7$ nm and 50.3 nm, with an increase in both the ensemble MSD (Fig. 4) and an increase in particle displacements with a λ of 98.0 nm and 169.0 nm, respectively (Fig. 5). We attribute the increase in λ and the corresponding displacements to the particles undergoing larger displacements in the regions of less crosslinked polymer network due to the addition of defects with increasing t_{hyd}. Conversely, in all these cases the middle portion of the van Hove follows Gaussian statistics representing immobile particles localized in primary cages, on the order of the instrumental resolution (~ 30 nm).

Figure 6 shows the non-Gaussian parameter (α_{NG}), a measure of the van Hove distribution function from Gaussian behavior, of the 15.1 nm PEG-functionalized QDs for $\langle\xi_s\rangle$ = 16.3, 21.3, 29.7 and 50.3 nm. For the most densely crosslinked network, $\langle\xi_s\rangle = 16.3$ nm, α_{NG} is relatively low at all measured τ, an average of 0.59 from $\tau = 0.03$ to 0.90 seconds. α_{NG} then monotonically increases with increasing $\langle\xi_s\rangle$, indicating that the nanoparticles experience a wider range of local environments as the number of and the size of the defects increases. As a result, the percentage of mobile particles and the magnitude of displacements increases as $\langle\xi_s\rangle$ increases, resulting in a broader distribution of dynamics due to the structural heterogeneity the particles experience. While α_{NG} values for $\langle\xi_s\rangle = 16.3$ nm, 29.7 nm and 50.3 nm are relatively constant for the examined range of τ, there is a decrease in α_{NG} for $\langle\xi_s\rangle = 21.3$ nm near 0.30 seconds. This is likely due to the smaller number of mobile particles that can be visualized across the τ range. As a result, the population of nanoparticles observed is biased toward slower moving (immobile) particles that are in the more homogeneous network region. The resulting decrease in α_{NG} is denoted by the open circles in Figure 6. This trend is not observed in the other networks because they contain a higher number of mobile particles.

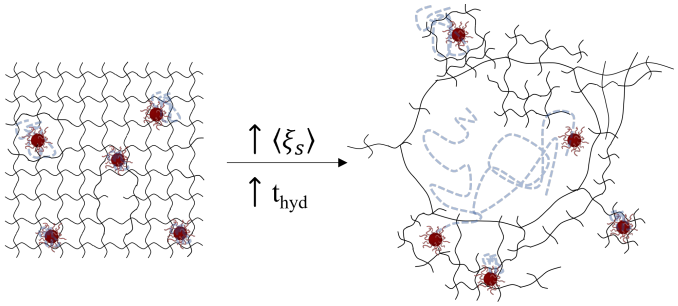

Fig. 7 Schematic of single nanoparticle ($d_h = 15.1$ nm) dynamics within nearly homogeneous hydrogels (left) and defective hydrogel networks (right). Immobile particles are trapped, whereas heterogeneity in defective hydrogels provides open paths for large displacements.

In the tetra-PEG hydrogels for all $\langle\xi_s\rangle$, the percentage of mobile 15.1 nm nanoparticles is relatively low. Even in the most defective networks where the nanoparticle diameter (15.1 nm) is over three times smaller than the $\langle\xi_s\rangle$ of 50.3 nm, only $\sim 7.5\%$ of the particles are mobile. We hypothesize that this is due to the wide range of ξ_s, with regions of high crosslinking density regions that immobilize nanoparticles even with a large $\langle\xi_s\rangle$ as shown in Figure 7.

3.3 Effect of particle size

To explore the sensitivity of probe size to the addition of defects and to determine if the confinement ratio (*CR*) can predict particle dynamics, we compare the mobility of 15.1 nm PEG-functionalized QDs with that of smaller 9.6 nm PEG-functionalized QDs and larger 47.1 nm polystyrene (PS) nanoparticles. First, we investigate if large particles exhibit mobility in the reaction-tuned hydrogels using fluorescent polystyrene (PS) nanoparticles, $d_h = 47.1$ nm. We note that the *CR* for these particles is > 1 for all but for the most highly disrupted hydrogel samples prepared here. As seen in the ensemble MSDs, the PS nanoparticles are immobile for all $\langle\xi_s\rangle$, indicating that even with the increasing number of defects in the network, the open regions are not large enough to allow for large displacements (over

200 nm) of the 47.1 nm PS as seen in Figure 8 (top row). Additionally, for a given $\langle \xi_s \rangle$, the breadth and shape of the van Hove distribution functions does not change with increasing τ, further indicating that the PS nanoparticles are immobile (see ESI †). While there are small changes in breadth of the exponential tails indicating that increasing $\langle \xi_s \rangle$ could be resulting in increased mobility within a cage, the difference in λ at $\tau = 0.3$ seconds between $\langle \xi_s \rangle = 16.3$ nm and 50.3 nm minutes is only ~ 3 nm, indicating that these are small changes in the primary cage size. This indicates that the defects and changes to the mesh size are relatively localized and small, as the defects are not large enough to induce the mobility of the larger PS particles.

Conversely, smaller quantum dots ($d_h = 9.6$ nm) with $CR < 1$ show increased sensitivity to the presence of these nanoscale defects. As shown in Figure 8 (bottom), for the most densely crosslinked network most of the smaller particles are immobile. However, unlike the larger QDs and the PS nanoparticles, there is a substantial percentage of mobile particles, 25.3%. The percentage of mobile particles increases with increasing $\langle \xi_s \rangle$ to 42.4% and 67.6% at 21.3 nm and 29.7 nm, respectively, before decreasing to 63.0% at 50.3 nm. This apparent decrease in mobile particles is attributed to rapidly moving nanoparticles in the open network. As a result, the nanoparticles diffuse out of the imaging plane within a few τ and thus cannot be tracked for extended τ (e.g. 0.1 second). At a singular $\langle \xi_s \rangle$, the breadth of the exponential tails increase with increasing τ, consistent with mobile particles (Fig. 9, inset). The characteristic decay length of the exponential tails also increases with larger $\langle \xi_s \rangle$, with λ increasing from 106.1 nm to 260.1 nm as $\langle \xi_s \rangle$ increases from 16.3 nm to 21.3 nm (Fig. 9). Similar to the trend seen with the 15.1 nm QDs, λ increases with larger $\langle \xi_s \rangle$, attributed to particles exploring regions of lower crosslinking density.

To avoid systems with biased statistics (e.g. particles diffusing rapidly out of the imaging plane), we compare dynamics in the same network ($\langle \xi_s \rangle = 21.3$ nm) for all nanoparticle sizes. Figure 10 shows both the MSDs of individual particle trajectories and a normalized distribution of individual MSDs at $\tau = 0.15$ seconds. As previously described, all of the larger PS particles are immobile as evidenced by both the nearly constant and low MSD values and a narrow distribution of MSDs around the ensemble average (top row). Similarly, the 15.1 nm QDs are primarily immobile, though as can be seen in the individual MSDs and in the MSD distribution that some particles are mobile (middle row). For the smallest QDs, there is a dramatic change in the mobility as shown by the two distinct populations of mobile particles, which appear as two distinct MSD at $\tau = 0.15$ seconds (bottom row). This increase in mobile particles indicates that the smaller particles are more sensitive to changes in the mesh size resulting from the formation of defects. We hypothesize that this size dependence is due to larger particles requiring a higher concentration of defects in a given spatial location to escape their localized cage compared to their smaller counterparts, resulting in an increased percentage of smaller QDs that are mobile in comparable networks. The dynamics as a function of nanoparticle size in the same defective network is schematically represented in Figure 10, where larger probes exhibit limited mobility compared to their smaller counterparts. This ability of these defective networks to trap large particles while allowing for smaller particles to diffuse could be used for size separation of polydisperse particles. Conversely, it also highlights how different sized particles can be used to investigate defective networks, as different size particles exhibit a wide range of dynamics.

While the confinement ratio may be a useful parameter to predict the onset of particle mobility, it may not fully explain the mobility of the nanoparticles in these defective networks. Even under apparently non-confining condition (e.g. 15.1 nm QD in a network with $\langle \xi_s \rangle = 50.3$ nm, CR = 0.30), a large portion of particles appear immobile. This trapping is likely due to highly crosslinked regions that restrict probe mobility, and more open regions encapsulating a high density of defects that are further pronounced by swelling. Interestingly, for even the most open network structures ($\langle \xi_s \rangle$ = 50.3 nm), the PS (47.1 nm) particles are found to be immobile, indicating that while the network is defective, the mesh sizes resulting from defects are not large enough to allow for large particle mobility, at least on the time scale of our imaging. Conversely, smaller particles are much more sensitive to changes in the structure and the introduction of defects, which can be seen by a subset of particles that are able to move within the gel, although again, a substantial number of particles remain trapped and localized within the network in the high crosslinking density (i.e. low defect) regions.

These results also suggest that CR alone does not capture particle dynamics. Table 1 shows that CR ranges from 2.89 to 0.19, and similar CRs exist for different particle-network systems. For example, the 47.1 nm PS nanoparticles in the most open network ($\langle \xi_s \rangle = 50.3$ nm) and 15.1 nm QDs in the dense network ($\langle \xi_s \rangle = 16.3$ nm) have similar CR ($d_h / \langle \xi_s \rangle = 0.94$ and 0.93, respectively). In both cases, all particles are immobile. However, for the smallest QDs (9.6 nm) in the nearly homogeneous network ($\langle \xi_s \rangle = 16.3$ nm) the percentage of mobile particles is over three times larger than that of the larger QDs (15.1 nm) in a defective network ($\langle \xi_s \rangle = 29.7$ nm). This is even though the CR in the 9.6 nm QD and $\langle \xi_s \rangle = 16.3$ nm network is larger (i.e. more confined) than that of the 15.1 nm QD in $\langle \xi_s \rangle = 29.7$ nm network, $CR = 0.59$ versus 0.51, respectively. Furthermore, the diffusion coefficient, taken from the linear portion of the ensemble MSD, of the smaller 9.6 nm QDs in the more confining network is approximately an order of magnitude higher than that of the larger particles in a more defective network, 4.4×10^3 nm^2/s compared to 4.9×10^2 nm^2/s. Interestingly, the value of λ at $\tau = 0.15$ seconds are similar, 107.5 nm and 106.1 nm (c.f. Figs. 5 and 9). This suggests that the distribution of mobile particle displacements is similar for both systems and that the increased diffusion coefficient comes primarily from the increase in mobile particles, not necessarily increased displacements. Systematic studies with systems that have identical confinement ratios in both nearly homogeneous (low defect) and more heterogeneous (high defect) networks are necessary to understand this preliminary finding. Overall, this indicates that particle dynamics in defective networks cannot fully be described by the average mesh size, $\langle \xi_s \rangle$, and by proxy the confinement ratio, CR. To fully capture the dynamics of particles in these systems, the mesh size as well as the network hetero-

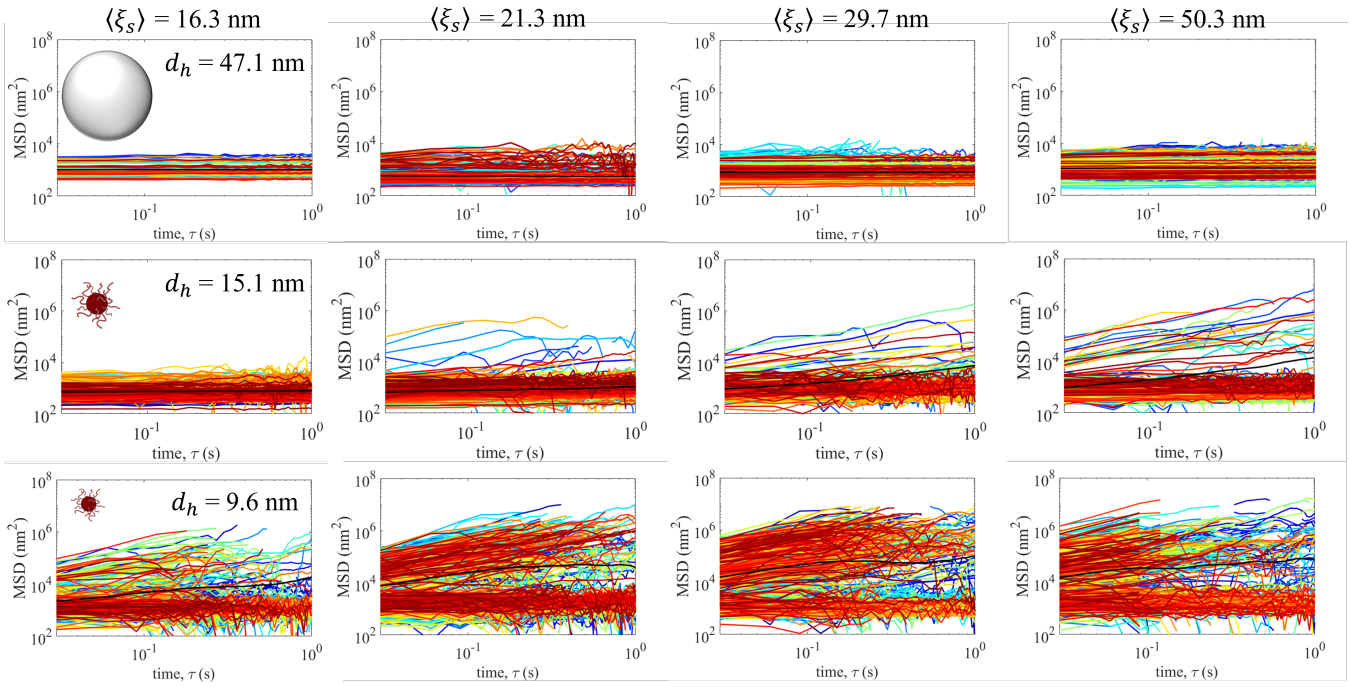

Fig. 8 Mean squared displacement (MSD) of individual 47.1 nm polystyrene nanoparticles (top row), 15.1 nm PEG-functionalized quantum dots (QD) (middle row) and 9.6 nm PEG-functionalized QDs (bottom row) for $\langle \xi_s \rangle = 16.3$ nm, 21.3 nm, 29.7 nm, and 50.3 nm. Black line represents the ensemble average MSD.

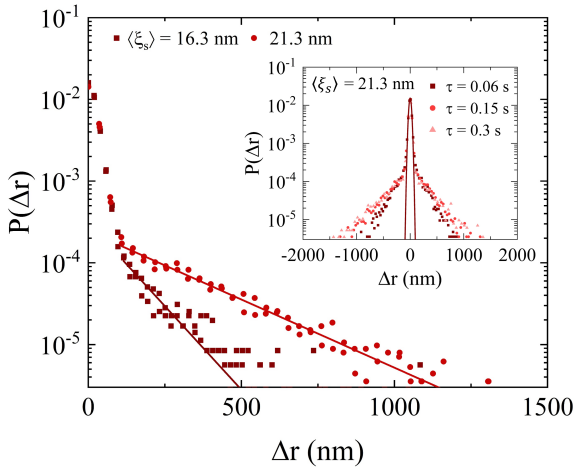

Fig. 9 van Hove distribution function of 9.6 nm PEG-functionalized quantum dot (QD) nanoparticles for $t_{hyd} = 0$ and 30 minutes at $\tau = 0.15$ seconds. Inset shows the van Hove distribution function for $t_{hyd} = 0$ minutes as a function of τ, at $\tau = 0.06, 0.15$ and 0.3 seconds. Line shows a Gaussian fit to $\tau = 0.06$ seconds.

geneity due to the density and distribution of defects should be considered.

4 Conclusions

In this study, tetra-PEG hydrogels with an increasing number of dangling ends are synthesized to examine the effect of defects on nanoparticle dynamics. Hydrogels with defects are prepared via reaction tuning, where the TPEG-SG macromonomer is partially degraded in buffer via hydrolysis of the NHS end group for increasing amount of time (t_{hyd}) prior to mixing with TPEG-A. For 15.1 nm PEG-functionalized QDs, there is limited mobility in the most densely crosslinked network where the average swollen mesh size ($\langle \xi \rangle = 16.3$ nm) is similar to the hydrodynamic diameter of the probe. As the number of defects is increased resulting in an increased average swollen mesh size, $\langle \xi \rangle = 21.3$ nm, 29.7 nm and 50.3 nm, as measured through rheology and swelling measurements, QDs mobility increases although a majority of the particles remain immobile. Due to the wide range of local environments, leading to both immobile and highly mobile particles, the particle dynamics in the more defective networks are heterogeneous. To determine the effect of nanoparticle size on probe dynamics in the defective hydrogels, 47.1 nm PS and 9.6 nm PEG-functionalized QDs are investigated. While there are limited changes between networks with $\langle \xi \rangle = 16.3$ nm and 50.3 nm for the large PS particles, the smaller QDs are sensitive to small perturbations in the hydrogel mesh as a function of reaction-tuning, exhibiting increased dynamics compared to the 15.1 nm QDs even in networks with comparable confinement ratios. This study informs the design of degradable hydrogels for biomedical applications, highlighting the importance of probe size for

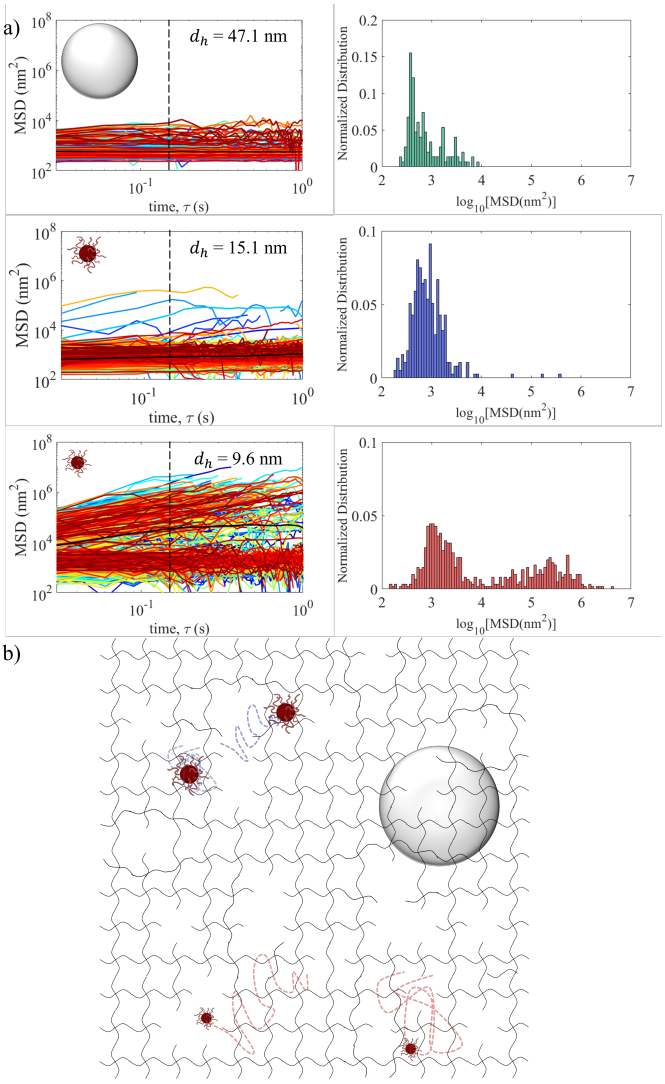

Fig. 10 a) Mean squared displacements (MSD) of 47.1 nm polystyrene (top) and 15.1 nm (middle) and 9.6 nm (bottom) PEG-functionalized quantum dots for $t_{hyd} = 30$ minutes ($\langle \xi_s \rangle = 21.3$ nm). Black solid lines indicate the ensemble average MSD and black dashed lines are a guide to the eye at $\tau = 0.15$ seconds. (left) Normalized distribution of individual MSDs at $\tau = 0.15$ seconds. (right). b) Schematic of nanoparticle dynamics for different nanoprobe sizes (bottom).

extended-release profiles of pharmaceutical containing nanoparticles. Furthermore, this study also serves as motivation to examine the dynamics of nanoparticle probes in nearly homogeneous and defective hydrogel networks with similar confinement ratios to further investigate the relationship between nanoparticle confinement and network heterogeneity due to defects.

Author Contributions

Katie Rose: Conceptualization, Methodology, Formal Analysis, Investigation, Writing - Original Draft, Visualization, **Emanuele Marino**: Resources, Writing - Review and Editing, **Christopher S. O'Bryan**: Formal Analysis, Visualization, Writing - Review and Editing, **Christopher B. Murray**: Resources, Writing - Review and Editing, Funding Acquisition, **Daeyeon Lee**: Conceptualization, Writing - Review and Editing, Supervision, Project Administration, Funding Acquisition, **Russell J. Composto**: Conceptualization, Writing - Review and Editing, Supervision, Project Administration, Funding Acquisition

Conflicts of interest

There are no conflicts to declare.

Acknowledgements

The authors thank Dr. Matthew Brukman and Dr. Jamie Ford for instrument support in the Singh Center for Nanotechnology. Support was provided by the NSF-PIRE-OISE-1545884 (RJC, DL, CBM, KAR), NSF Graduate Fellowships (KAR), NSF-POLYMERS-DMR-1905912 (RJC), NSF-MRSEC-DMR 1720530 (CBM, DL), NSF-DMR-2019444 (EM, CBM) and NSF-CBET-2034122 (RJC). Particle tracking experiments were performed at the Scanning and Local Probe Facility at the Singh Center for Nanotechnology at the University of Pennsylvania, supported by NSF-MRSEC-DMR-1720530.

Notes and references

1 S. Khetan, J. S. Katz and J. A. Burdick, *Soft Matter*, 2009, **5**, 1601–1606.
2 P. Matricardi, C. Di Meo, T. Coviello, W. E. Hennink and F. Alhaique, *Advanced Drug Delivery Reviews*, 2013, **65**, 1172–1187.
3 C. H. Park and I. Orozco-Avila, *Biotechnol. Prog.*, 1992, **8**, 6.
4 Y. Liang, J. He and B. Guo, *ACS Nano*, 2021, **15**, 12687–12722.
5 E. A. Kamoun, E.-R. S. Kenawy and X. Chen, *Journal of Advanced Research*, 2017, **8**, 217–233.
6 Y. Wang, J. Wang, Z. Yuan, H. Han, T. Li, L. Li and X. Guo, *Colloids and Surfaces B: Biointerfaces*, 2017, **152**, 252–259.
7 J. Henise, B. R. Hearn, G. W. Ashley and D. V. Santi, *Bioconjugate Chemistry*, 2015, **26**, 270–278.
8 S. Sheth, E. Barnard, B. Hyatt, M. Rathinam and S. P. Zustiak, *Frontiers in Bioengineering and Biotechnology*, 2019, **7**, 410.
9 K. R. Kamath and K. Park, *Advanced Drug Delivery Reviews*, 1993, **11**, 59–84.
10 F. Di Lorenzo and S. Seiffert, *Polymer Chemistry*, 2015, **6**, 5515–5528.

11 T. Matsunaga, T. Sakai, Y. Akagi, U. I. Chung and M. Shibayama, *Macromolecules*, 2009, **42**, 1344–1351.

12 A. M. Hecht, R. Duplessix and E. Geissler, *Macromolecules*, 1985, **18**, 2167–2173.

13 M. Shibayama, *Macromolecular Chemistry and Physics*, 1998, **199**, 1–30.

14 J. Bastide and L. Leibler, *Macromolecules*, 1988, **21**, 2647–2649.

15 K. Saalwachter, *Progress in Nuclear Magnetic Resonance Spectroscopy*, 2007, **51**, 1–35.

16 K. Saalwächter, *Journal of the American Chemical Society*, 2003, **125**, 14684–14685.

17 C. H. Lee, A. J. Crosby, T. Emrick and R. C. Hayward, *Macromolecules*, 2014, **47**, 741–749.

18 E. Parrish, M. A. Caporizzo and R. J. Composto, *The Journal of Chemical Physics*, 2017, **146**, 203318.

19 K. J. A. Martens, J. van Duynhoven and J. Hohlbein, *Langmuir*, 2020, **36**, 5502–5509.

20 T. Sakai, T. Matsunaga, Y. Yamamoto, C. Ito, R. Yoshida, S. Suzuki, N. Sasaki, M. Shibayama and U.-i. Chung, *Macromolecules*, 2008, **41**, 5379–5384.

21 T. Sakai, *Reactive and Functional Polymers*, 2013, **73**, 898–903.

22 F. Lange, K. Schwenke, M. Kurakazu, Y. Akagi, U.-i. Chung, M. Lang, J.-U. Sommer, T. Sakai and K. Saalwächter, *Macromolecules*, 2011, **44**, 9666–9674.

23 M. Kurakazu, T. Katashima, M. Chijiishi, K. Nishi, Y. Akagi, T. Matsunaga, M. Shibayama, U.-i. Chung and T. Sakai, *Macromolecules*, 2010, **43**, 3935–3940.

24 K. Nishi, K. Fujii, Y. Katsumoto, T. Sakai and M. Shibayama, *Macromolecules*, 2014, **47**, 3274–3281.

25 K. Nishi, M. Chijiishi, Y. Katsumoto, T. Nakao, K. Fujii, U.-i. Chung, H. Noguchi, T. Sakai and M. Shibayama, *The Journal of Chemical Physics*, 2012, **137**, 224903.

26 Y. Akagi, T. Katashima, H. Sakurai, U.-i. Chung and T. Sakai, *RSC Advances*, 2013, **3**, 13251.

27 Y. Akagi, H. Sakurai, J. P. Gong, U.-i. Chung and T. Sakai, *The Journal of Chemical Physics*, 2013, **139**, 144905.

28 T. Sakai, Y. Akagi, S. Kondo and U. Chung, *Soft Matter*, 2014, **10**, 6658–6665.

29 K. Khairulina, X. Li, K. Nishi, M. Shibayama, U.-i. Chung and T. Sakai, *The Journal of Chemical Physics*, 2015, **142**, 234904.

30 K. Khairulina, U.-i. Chung and T. Sakai, *Journal of Materials Chemistry B*, 2017, **5**, 4526–4534.

31 D. A. Hanifi, N. D. Bronstein, B. A. Koscher, Z. Nett, J. K. Swabeck, K. Takano, A. M. Schwartzberg, L. Maserati, K. Vandewal, Y. van de Burgt, A. Salleo and A. P. Alivisatos, *Science*, 2019, **363**, 1199–1202.

32 E. Marino, S. W. van Dongen, S. J. Neuhaus, W. Li, A. W. Keller, C. R. Kagan, T. E. Kodger and C. B. Murray, *Chemistry of Materials*, 2022, **34**, 2779–2789.

33 E. Parrish, K. A. Rose, M. Cargnello, C. B. Murray, D. Lee and R. J. Composto, *Soft Matter*, 2020, **16**, 2256–2265.

34 M. S. Rehmann, K. M. Skeens, P. M. Kharkar, E. M. Ford, E. Maverakis, K. H. Lee and A. M. Kloxin, *Biomacromolecules*, 2017, **18**, 3131–3142.

35 F. Ruhnow, D. Zwicker and S. Diez, *Biophysical Journal*, 2011, **100**, 2820–2828.

36 N. Tarantino, J.-Y. Tinevez, E. F. Crowell, B. Boisson, R. Henriques, M. Mhlanga, F. Agou, A. Israël and E. Laplantine, *Journal of Cell Biology*, 2014, **204**, 231–245.

37 A. Rahman, *Physical Review*, 1964, **136**, A405–A411.

38 Y. Akagi, T. Katashima, Y. Katsumoto, K. Fujii, T. Matsunaga, U.-i. Chung, M. Shibayama and T. Sakai, *Macromolecules*, 2011, **44**, 5817–5821.

39 H. H. Winter, *Polymer Engineering & Science*, 1987, **27**, 1698–1702.

40 C.-Y. M. Tung and P. J. Dynes, *Journal of Applied Polymer Science*, 1982, **27**, 569–574.

41 G. Stojkov, Z. Niyazov, F. Picchioni and R. K. Bose, *Gels (Basel, Switzerland)*, 2021, **7**, 255.

42 A. C. Jimenez-Vergara, J. Lewis, M. S. Hahn and D. J. Munoz-Pinto, *Journal of Biomedical Materials Research Part B: Applied Biomaterials*, 2018, **106**, 1339–1348.

43 L.-H. Cai, S. Panyukov and M. Rubinstein, *Macromolecules*, 2015, **48**, 847–862.

44 B. P. Bhowmik, I. Tah and S. Karmakar, *Physical Review E*, 2018, **98**, 022122.

45 M. T. Valentine, P. D. Kaplan, D. Thota, J. C. Crocker, T. Gisler, R. K. Prud', M. Beck and D. A. Weitz, *Physical Review E*, 2001, **64**, 061506.